PCCP

Role of tilt grain boundaries on the structural integrity of WSe2 monolayers

Journal:	*Physical Chemistry Chemical Physics*
Manuscript ID	CP-ART-07-2022-003492.R1
Article Type:	Paper
Date Submitted by the Author:	30-Sep-2022
Complete List of Authors:	Sakib, Nuruzzaman; The University of Alabama, Mechanical Engineering; Shahjalal University of Science and Technology, Mechanical Engineering Paul, Shiddartha; University of Illinois at Urbana-Champaign, Department of Mechanical Science and Engineering Nayir, Nadire; Pennsylvania State University van Duin, Adri; The Pennsylvania State University, Mechanical and Nuclear Engineering Neshani, Sara ; The University of Alabama Momeni, Kasra; The University of Alabama System, Mechanical Engineering ; The University of Alabama, Mechanical Engineering

ARTICLE

Role of tilt grain boundaries on the structural integrity of WSe_2 monolayers

Received 29th July 2022,
Accepted 00th January 20xx

DOI: 10.1039/x0xx00000x

Nuruzzaman Sakib[a,b], Shiddartha Paul[c], Nadire Nayir[d,e], Adri C.T. van Duin[e], Sara Neshani[f], Kasra Momeni[a,†]

Transition metal dichalcogenides (TMDCs) are potential materials for future optoelectronic devices. Grain boundaries (GBs) can significantly influence the optoelectronic properties of TMDC materials. Here, we have investigated tungsten diselenide (WSe_2) monolayers' mechanical characteristics and failure process with symmetric tilt GBs using ReaxFF molecular dynamics simulations. In particular, the effect of topological defects, loading rate, and temperature are investigated. We considered nine different grain boundary structures of monolayer WSe_2, of which six are armchair (AC) tilt, and the remaining three are zigzag (ZZ) tilt structures. Our results indicate both tensile strength and fracture strain of WSe_2 with symmetric tilt GBs fall as the temperature rises. We revealed an interfacial phase transition for high-angle GBs reduces the elastic strain energy within the interface at finite temperatures. Furthermore, brittle cracking is the dominant failure mode in the WSe_2 monolayer with tilted GBs. WSe_2 GB structures showed more strain rate sensitivity at high temperatures than at low temperatures.

Introduction

Multi-layered materials show strong chemical bonds within the layer but weak van der Waals forces in between [1], which allows these materials to be physically or chemically thinned to a single atomic two-dimensional (2D) layer [2]. The synthesis of 2D materials has become critical in modern materials research [3–13] because of their unique physicochemical properties that differ from their bulk counterparts. Specifically, these materials with defined geometries exhibit unique shape-dependent properties and have been successfully used in nanoelectronics devices [14]. In the 2D materials family, graphene is immensely popular because of its several unique features, such as thermal conductivity, visual transparency, and elastic properties [15–17] that motivated several studies investigating its mechanochemistry.[18,1920] However, the absence of an electronic bandgap [21] has motivated a drive for synthesizing 2D materials with semiconducting capabilities, including TMDCs. These materials have attracted significant attention because of their natural abundance and semiconducting capabilities among 2D materials [22].

Tungsten diselenide (WSe_2), a TMDC, is an excellent option for semiconducting applications [23–27]. It comprises one layer of W atoms sandwiched between two layers of Se atoms. Mechanical exfoliation,[28,29] and chemical vapor deposition (CVD) [30–34] are two main fabrication methods of WSe_2. Like all other materials, WSe_2 has a variety of defects, including edges, vacancies, adatoms, substitutional impurities, and GBs, all of which significantly impact its characteristics [35–38]. GBs are a common form of defect in large-scale 2D material films synthesized by CVD, significantly impacting their characteristics [39]. Several studies have been performed to understand the role of defects on the characteristics of various 2D materials. Mechanical characteristics of the pristine and air-aged high-quality WS_2, WSe_2, and WTe_2 were investigated using the indentation method [40], demonstrating that WS_2's mechanical properties degraded the most with thickness. The mechanical properties of Graphene-WSe_2 vertical heterostructures are also studied using the MD technique [41], indicating direction-dependent fracture processes, where the WSe_2 sheet transformed from h-WSe_2 to t-WSe_2 upon loading in the ZZ direction. In another study on MoS_2, it was shown that GB and vacancy defects degrade the mechanical characteristics of MoS_2. In contrast, vacancy inclusion at a small scale promotes plasticity in MoS_2 and reduces the tensile strength [42]. MD simulations were also used to investigate the effects of temperature, strain rate, and vacancies on the mechanical responses of h-WSe_2 and t-WSe_2 [43], indicating strain rate independence of the fracture strain, fracture strength, and Young's modulus of both h-WSe_2 and t-WSe_2. Furthermore, upon increasing the density of vacancies, the mechanical strength of both h-WSe_2 and t-WSe_2 reduced

[a] Department of Mechanical Engineering, University of Alabama, Tuscaloosa, AL, USA.
[b] Department of Mechanical Engineering, Shahjalal University of Science and Technology, Sylhet, Bangladesh.
[c] Department of Mechanical Science and Engineering, University of Illinois at Urbana-Champaign, Urbana, Illinois, USA.
[d] Physics department, Karamanoglu Mehmetbey University, Karaman, Turkey.
[e] Department of Mechanical Engineering and 2-Dimensional Crystal Consortium (2DCC) Materials Research Institute, The Pennsylvania State University, University Park, PA, USA.
[f] Department of Electrical Engineering, University of Alabama, Tuscaloosa, AL, USA
[†] Corresponding author: kmomeni@ua.edu
Electronic Supplementary Information (ESI) available: Additional simulation details, including the atomistic structure and additional calculation results. See DOI: 10.1039/x0xx00000x

due to the increase in the density of microcracks and disorganization of W-Se bonds.

Despite the aforementioned studies on the role of defects in 2D materials, a comprehensive study of the role of GB on mechanical characteristics in the WSe_2 monolayer is lacking. This topic is of paramount importance because all the largescale WSe_2 films are polycrystal. Thus, here we used ReaxFF MD simulations to investigate the role of tilt GBs on the mechanical characteristics of bi-crystal WSe_2 monolayers.

Methodology

We created ~27 nm × ~27 nm monolayer WSe_2 models containing symmetric AC tilt GBs of three different misorientation angles – i.e., 9.4°, 13.2°, and 21.8° – as shown in Figure 1. Unlike graphene, WSe_2 AC tilt GBs are of two types based on the bond shared by the pentagon-heptagon ring: (i) the Se-Se and (ii) the W-W bond shared pentagon-heptagon defect. They are identified as Se5|7 and W5|7, respectively. The Se-Se bond shared structures of symmetric AC tilt GB and the W-W bond shared structures of symmetric AC tilt GB for the three misorientation angles considered here are shown in Figures 1(a-c) and 1(d-f), respectively. The considered ZZ tilt

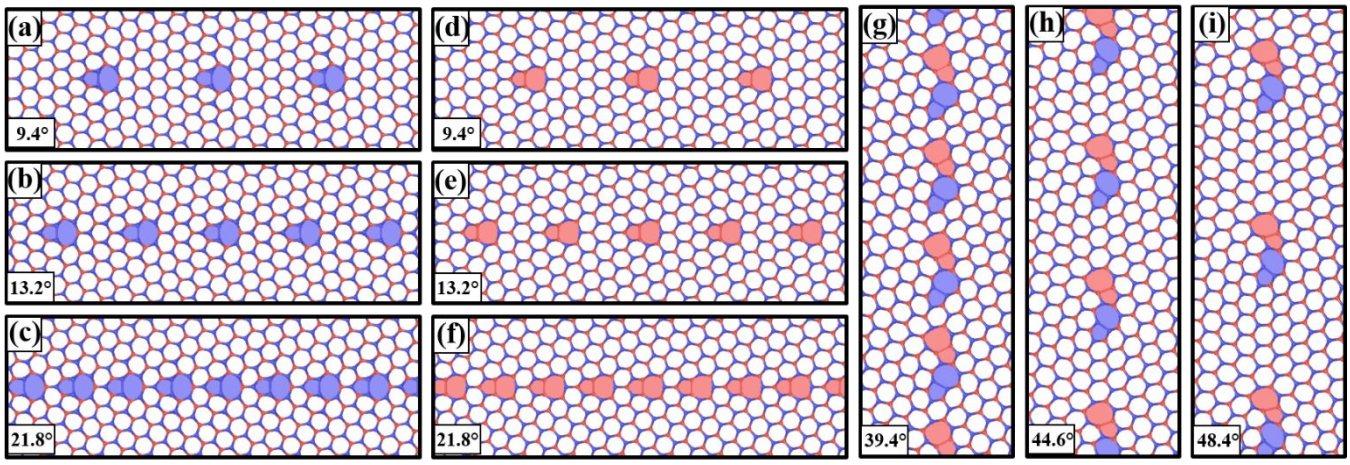

Figure 1. Monolayer WSe_2 GB structures. Se5|7 dislocations in AC tilt GBs with tilt angles of (a) 9.4°, (b) 13.2°, and (c) 21.8°; W5|7 dislocations in AC tilt GBs with tilt angles of (d) 9.4°, (e) 13.2°, and (f) 21.8°; ZZ tilt GBs made up of W5|7 + Se5|7 dislocations with tilt angles of (g) 39.4°, (h) 44.6°, and (i) 48.4°. W5|7 and Se5|7 dislocations in GBs are coloured in red and blue, respectively. Red circles represent W atoms, and blue circles represent Se atoms

W5|7 + Se5|7 structures are shown in Figures 1 (g-i). GBs were generated by rotating a WSe2 monolayer's unit cell at the necessary angle and converting it to its orthogonal cell. This structure was duplicated in the planer direction to reach ~150Å. Mirroring the structure created negative rotation. Stitching the two structures together and deleting duplicate atoms in the interface generated the GB. [44]. Removing duplicate atoms from planar image cells validated the periodicity of the boundary structure.

We created the GB by rotating two monolayers at the same angle but in opposite directions, stitching them together, deleting the overlapped atoms in the structure, and minimizing energy using the conjugate gradient method. We used 0.65 nm as the nominal thickness of monolayer WSe_2 structures [45]. All the structures are periodic in the plane of the monolayer WSe_2 to avoid the finite-size effects [46]. ReaxFF MD simulations are used to investigate the mechanical properties and the fracture mechanism of the bi-crystal WSe_2 monolayer. We used the Large-scale Atomic/Molecular Massively Parallel Simulator (LAMMPS) code to perform the simulations [47] with a time step of 0.25fs. Following the energy minimization, we relaxed the structures at simulation temperatures within the range of 10-300 K using the Nose-Hoover thermostat (NVT) for 12.5 ps and then using the Noose-Hoover barostat (NPT) for another 50 ps at atmospheric pressure and simulation temperatures ranging 10-300K. Damping constant for temperature and pressure is 50 fs and 1250 fs, respectively. The standard velocity-Verlet integrator is used to integrate the equations of motion. The structure's (virial) stress-strain behaviour is obtained by deforming the simulation box perpendicular to the GB direction in the NPT ensemble with an engineering strain rate of 10^9 s^{-1} compatible with other MD Studies [48,49]. As a result, the length of the simulation box along the GB was changed due to the Poisson's effect.

We used modified ReaxFF potential [45] to capture covalent bond breaking and formation by updating the bond order at each MD timestep. We validated the model by calculating the properties of pristine AC and ZZ WSe_2 under the NPT ensemble at 300K. We calculated Young's modulus of pristine ZZ and AC WSe_2 as 201GPa and 225 GPa, respectively, which agrees with the reported values [45]. We calculated an ultimate strength of 22GPa and 27GPa for ZZ and AC WSe_2 monolayers, respectively, which are comparable to the 23.7 GPa and 28.4 GPa values reported in the literature [45]. Young's modulus for the WSe_2 monolayer is found to be 201GPa using density functional theory calculations that are also comparable to our analyses [50]. The stress-strain response for pristine WSe_2 is presented in Figure S1 of the supporting material.

Results and discussion

Effect of internal stresses and strains

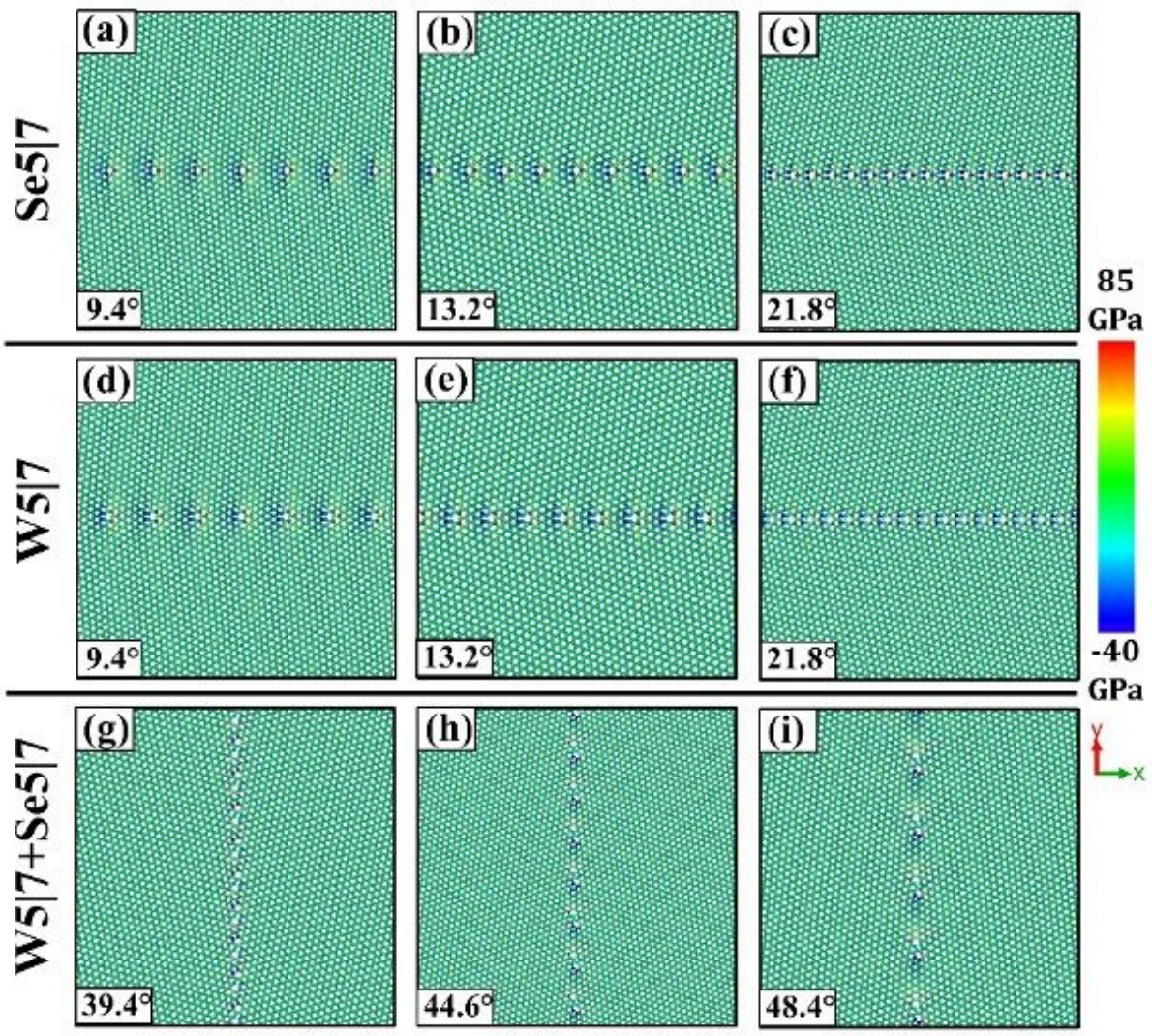

Figure 2. Atomic pre-stress due to the presence of the WSe_2 GB. (a) 9.4° Se5|7, (b) 13.2° Se5|7, (c) 21.8° Se5|7, (d) 9.4° W5|7, (e) 13.2° W5|7, (f) 21.8° W5|7, (g) 39.4° W5|7+Se5|7, (h) 44.6° W5|7+Se5|7, and (i) 48.4° W5|7+Se5|7. For Se5|7, the maximum compressive stress is experienced by the Se-Se bond; for W5|7, the W-W bond experiences the maximum compressive stress. Color-coded plots are generated by plotting per-atom stress in the normal to GB direction.

Failure of materials, including atomically thin WSe_2, is driven by the formation of microcracks, which are formed when stresses in the material increase beyond some critical stress, e.g., von Mises stress [51]. Thus, internal stresses strongly impact the formation and propagation of microcracks and, thus, the final strength of materials. WSe_2 monolayers are no exception. GBs are the microstructural features altering the internal stresses and thus determine monolayers' final properties. In contrast to the pristine WSe_2 monolayer structure, inter-atomic bond lengths are non-uniform in the tilt GB region, resulting in pre-strained bonds due to the presence of GB dislocations in the form of pentagon-heptagon (5|7) pair. From a geometric point of view, a 5|7 pair looks like a disclination dipole, which has two disclinations of opposite signs [52–54]. The pentagon defect is considered positive disclination, and the heptagon is considered negative disclination.

Grain boundaries may consist of evenly spaced disclination dipoles or dipole clusters. Here, we considered the evenly spaced disclination dipoles for AC and ZZ tilt GBs. The stress-volume component normal to the GB is plotted in Figure 2, i.e., σ_{yy} for the AC tilt GB, Figure 2(a-f), and σ_{xx} for the ZZ tilt GB, Figure 2(g-i). These contour plots show a similar trend reported for graphene GBs [55]. The stress volume unit is used here to avoid dealing with the controversies that may arise regarding a definition of volume for atomically thin structures. Compared to the hexagon ring bond length, the heptagon ring bonds are stretched, thus subjected to tensile stress, and the pentagon ring bonds are contracted and thus are subjected to compressive stress. Though several bonds are pre-stressed, the bond shared by the 5|7 ring experiences maximum compressive stress regardless of the misorientation angle. For Se5|7, the maximum compressive stress is experienced by the Se-Se bond, and maximum tensile stress is experienced by a single W atom of a heptagon, which has the longest distance from its nearest pentagon. For W5|7, the maximum compressive stress is experienced by the W-W bond, and maximum tensile stress is experienced by the double W atom of the heptagon. However, for graphene 5|7 dislocations, maximum stress was

experienced by the bond shared by the hexagon and heptagon ring [44].

Effect of grain boundary

GB structure for both the Se5|7 and W5|7 AC tilt GB structures, Figure 1.

For the ZZ tilt W5|7+Se5|7 structures, dislocation density is maximum for the 39.4° structure and minimum for the 48.4°

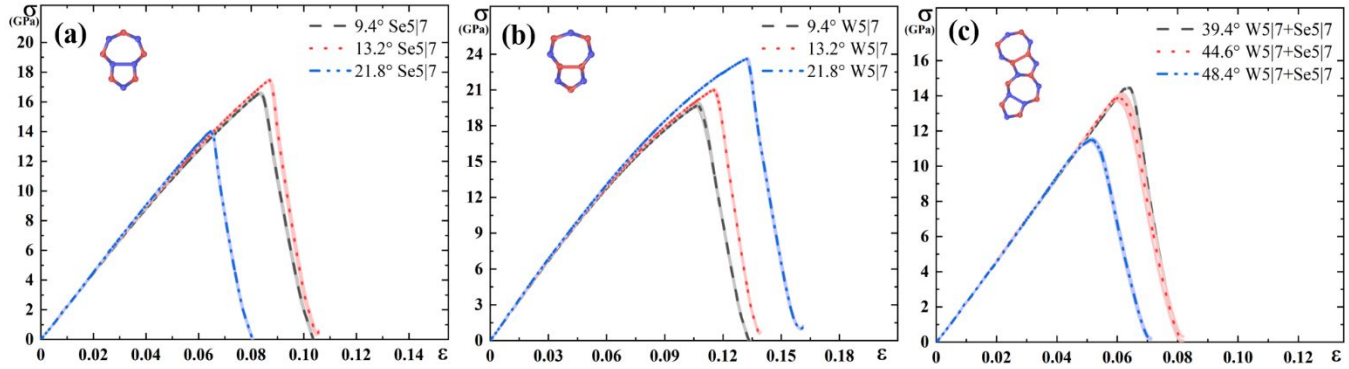

Figure 3. Stress (σ) – strain (ε) response of differently misoriented grains under uniaxial loading normal to GB direction at 10K temperature. (a) AC tilt Se5|7 structures, (b) AC tilt W5|7 structures, and (c) ZZ tilt W5|7+Se5|7 structures. Red circles represent W atoms, and blue circles represent Se atoms.

We have investigated the role of different GBs on the strength of bi-crystalline WSe_2 structures at low temperatures, where the effect of thermal fluctuations is negligible. The stress normal to GB vs. strain response of the structures is shown in Figure 3 for the AC tilt and ZZ tilt GBs at 10K temperature. We used three separate tensile loading simulations with different seed velocities for each GB to capture the correct statistics. Our simulations indicate an almost linear stress-strain correlation up to a critical point followed by a sudden drop in the finite strain regime, which is a brittle fracture characteristic.

The tensile strength of graphene sheets is higher for GBs with higher misorientation angles [56,57]. However, this behaviour was not observed [46] in a single-layer boron nitride nanosheet with tilted GBs. Here, for Se5|7 structures, the strength of low angle GBs, i.e., 9.4° and 13.2°, are relatively the same, while it suddenly drops for the 21.8° GB. The same conclusion can be made on the ZZ tilt W5|7+Se5|7 structures. For the W5|7 structures, the strength is ordered as 21.8°>13.2°>9.4°, i.e., there is a monotonic increase in strength with the misorientation. It indicates that the strength increases upon increasing the dislocation density, as the misorientation angle is correlated with the dislocation density. Dislocation density is maximum for the 21.8° GB structure and minimum for the 9.4° structure, Figure 1. With increasing dislocation density, the gap between disclination dipoles reduces. Thus, the stress field for one disclination dipole interferes with the stress field of the adjacent disclination dipole, resulting in a higher elastic energy density that alters the mechanical response of the material. However, by computing the stress-strain curves for different misoriented GBs in Figure 1, we can conclude that dislocation density is less critical in determining WSe_2's mechanical properties than the GBs chemistry. Although the Se5|7 GB with higher dislocation density has the lowest fracture strain, the same W5|7 GB has the highest fracture strain. In the case of W5|7+Se5|7 GB, the fracture stress is comparable with Se5|7 GB, which has the lowest fracture stress among Se5|7 and W5|7 GBs. It indicates that the strength of the GBs in WSe_2 is determined by the chemistry of the GB rather than dislocation density, where weaker bonds act as the bottleneck for the GB strength. We revealed the same trend in this work for Se5|7 and W5|7 GBs as to the AC tilt GB fracture strength of MoS_2 for S5|7 and Mo5|7 GB, respectively.[58]

The strain energy density (energy per atom), ψ^*, vs. strain at 10K is shown in Figure 4. Strain energy density is calculated as, ψ*= (Total Energy - Initial Total Energy) / (No. of atom), which follows a parabolic increase that is characteristic of a linear elastic deformation before reaches a max right before the

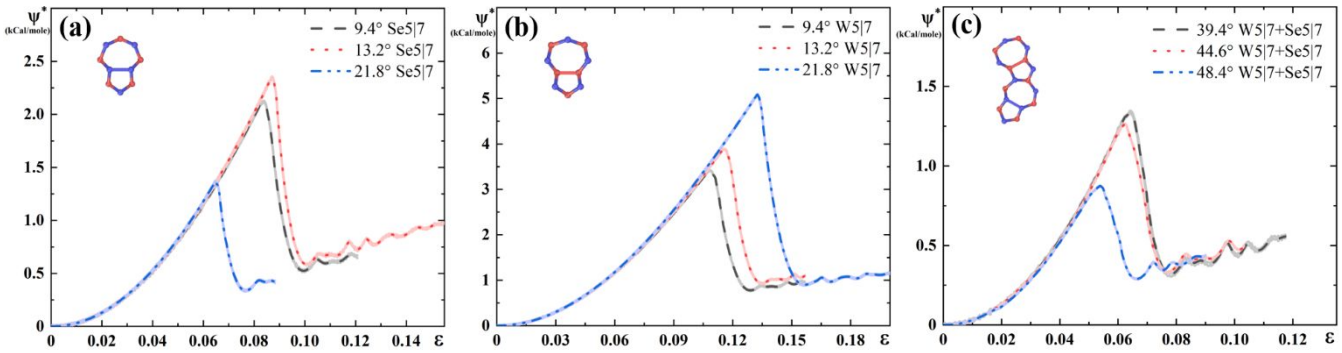

Figure 4. Strain energy per atom, ψ^*(kCal/mol), vs. strain (ε) for differently misoriented structures at 10K temperature. (a) AC tilt Se5|7 structures, (b) AC tilt W5|7 structures, and (c) ZZ tilt W5|7+Se5|7 structures. Red circles represent W atoms, and blue circles represent Se atoms.

sudden drop due to breaking of bonds. The W5|7 structures are also demonstrating a higher rigidity compared to the Se5|7 counterparts, where ψ^* of W5|7 monolayers are twice larger than Se5|7 structures.

Effect of temperature

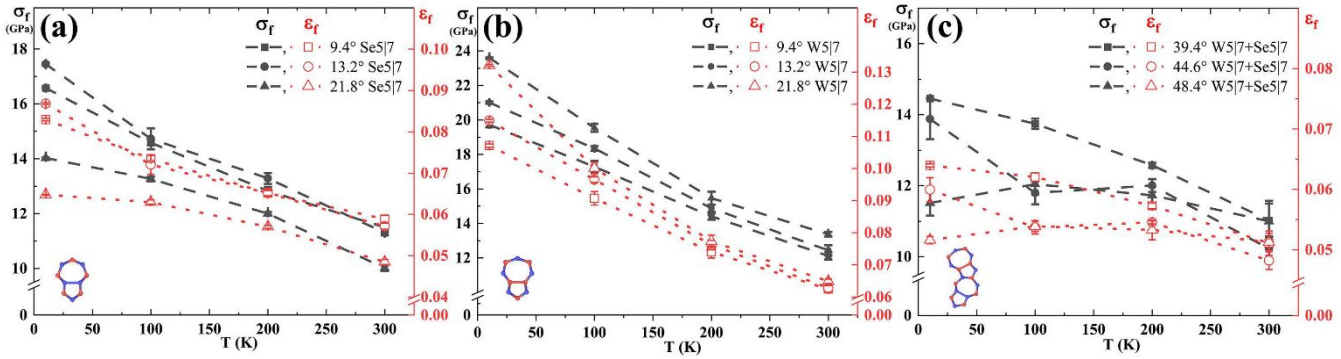

Figure 5. Effect of temperature on the fracture strength (σ_f) and fracture strain (ε_f) for different GB structures. (a) AC tilt Se5|7 GBs with misorientation angle of 9.4°, 13.2°, 21.8°, (b) AC tilt W5|7 GBs with misorientation angle of 9.4°, 13.2°, 21.8°, and (c) ZZ tilt W5|7+Se5|7 GBs with misorientation angles of 39.4°, 44.6°, 48.4°. The black and red lines indicate the fracture strength and strain curves with temperature, respectively. Red circles represent W atoms, and blue circles represent Se atoms.

We performed tensile test simulations at 10K, 100K, 200K, and 300K to understand the effect of temperature on the mechanical behaviour of WSe_2 structures with different GBs. The stress-strain curves for all the structures at the selected temperatures are shown in Figures S2-S4 in the Supplementary Information. Variation of fracture strength, σ_f, and fracture strain, ε_f, with temperature are shown in Figure 5 for the AC tilt Se5|7 and W5|7, and ZZ tilt W5|7+Se5|7 structures. We observed that σ_f and ε_f reduced for all the GB structures upon increasing temperature. The effect of temperature on σ_f and ε_f follows a similar trend reported for bigrain [59] and pristine [60] graphene's. This behaviour can be explained by the thermally activated debonding process, where the thermal fluctuation energy contributes to the energy necessary for the nucleation and propagation of microcracks.

The effect of temperature on Young's modulus, E, is shown in Figure 6 for the AC tilt Se5|7 and W5|7 GBs, and ZZ tilt W5|7+Se5|7 GBs. Our results indicate a weak correlation between Young's modulus and temperature for the AC tilt Se5|7 structures compared to the W5|7 structures. There is not a statistically significant difference between E values of differently misoriented GBs at various temperatures (Figure 6a). However, in the case of W5|7 GBs, the 9.4° GB has the lowest E value at all temperatures. There is no statistically meaningful difference between 13.2° and 21.8° W5|7 GBs beyond 100K. Furthermore, the 9.4° Se5|7 and W5|7 GBs have the relatively same elastic modulus, while 13.2° and 21.8° W5|7 GBs have a higher Young's modulus compared with the corresponding Se5|7 GBs.

In the case of high angle W5|7+Se5|7 mixed GBs, we revealed a complex variation in E at different temperatures. Although E drops upon increasing temperature for all the considered high angle GBs, the rate of reduction in the elastic modulus is different for each GB. Among the three GBs, the 46.4° W5|7+Se5|7 GB has the largest drop in E upon increasing temperature greater than 100K, which remains statistically constant up to room temperature. This drop is due to the structural change of GBs at high temperatures, shown in the Supplementary Information Figure S7. Increasing temperature for the high-angle GBs (44.6° and 48.4°) results in dissociation of two adjacent 5|7 dislocations into separated intermediate 8|6 dislocations, followed by transformation into a tetragonal and horizontal 5|7 dislocation pair. This transformation allows the sharp angle in the high-angle bi grain structure to split into two low angle boundaries with a large angle between the crystals within the GB width, resulting in the relaxation of the interfacial stresses. The lowest rate of softening vs. temperature is for 39.4° W5|7+Se5|7 GB. Although it has the

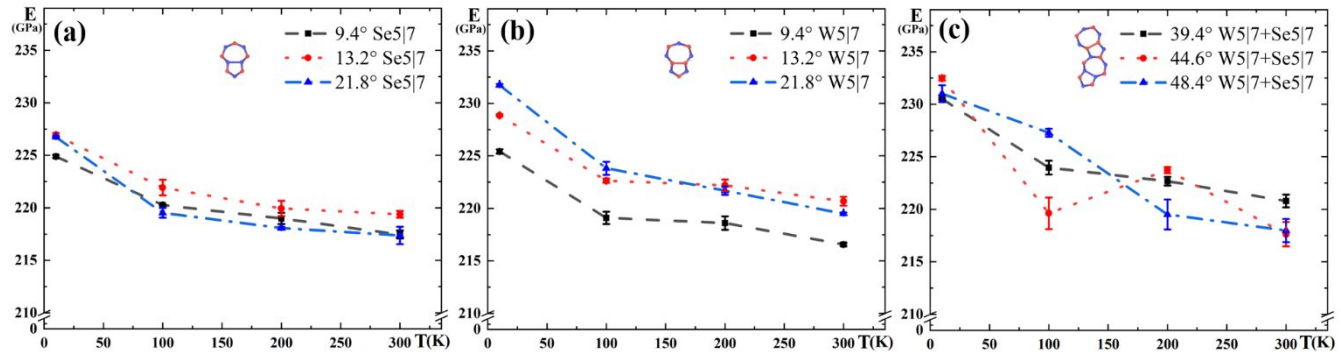

Figure 6. Effect of temperature on Young's modulus for different GB structures. (a) AC tilt Se5|7 structures with misorientation angles of 9.4°, 13.2°, 21.8°, (b) AC tilt W5|7 structures with misorientation angles of 9.4°, 13.2°, 21.8°, and (c) ZZ tilt W5|7+Se5|7 structures with misorientation angles of 39.4°, 44.6°, 48.4°.

lowest E value at 10K, it becomes the stiffest structure at room temperature. The calculated Young's modulus, E of these structures is consistent with reported values [45,50,61]. In fact, Young's modulus for the pristine WSe_2 and the structures having different GB misorientations lies in the same, indicating the GBs do not impact Young's modulus.

Effect of strain rate

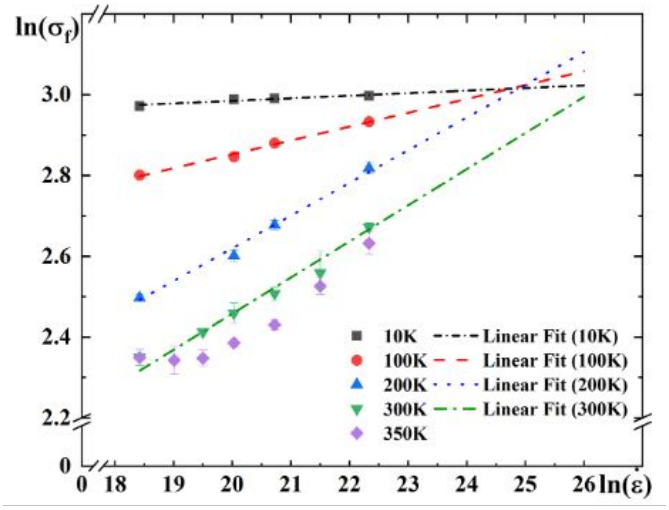

Figure 7. Variation of fracture strength of 9.4° W5|7 GB with strain rate on a logarithmic scale. Low strain sensitivity is observed at low temp, which increases upon increasing temperature and a constant slope for T>200K.

The strain rate is a crucial factor determining the mechanical properties of materials. Although the classical MD technique is inherently limited to very high strain rates, yet it can provide an insight to the mechanical behaviour of the material upon considering different strain rates. We performed uniaxial tensile test simulations at different strain rates to address the effect of strain rate sensitivity, for the AC tilt W5|7 GB with 9.4° misorientation angle at 10K, 100K, 200K, 300K, and 350K. The strain rates selected for these simulations are $10^8 s^{-1}$, $5\times10^8 s^{-1}$, $10^9 s^{-1}$, and $5\times10^9 s^{-1}$. Statistical results are obtained by running three sets of simulations at the same temperature with different seed velocities.

The effect of strain rate on the strength of the material is evaluated using an Arrhenius type equation [62]

$$\dot{\varepsilon} = A\sigma^{\frac{1}{m}} e^{-\frac{Q}{RT}} \quad (1)$$

Here, *m* is the strain rate sensitivity. *A* is a constant, and *R* is the universal gas constant r. $\dot{\varepsilon}$, σ, Q, and T are the strain rate, fracture strength, activation energy, and temperature, respectively. From Eq. (1), by taking the natural logarithm, we have

$$\ln(\dot{\varepsilon}) = \ln(A) + \frac{1}{m}\ln(\sigma) - \frac{Q}{RT}. \quad (2)$$

Partial differentiation of Eq. (2) assuming T as a constant, as the simulations were performed at controlled temperatures, we have

$$m = \frac{\partial \ln(\sigma)}{\partial \ln(\dot{\varepsilon})} \quad (3)$$

Therefore, taking the slope of the $\ln(\sigma)$ versus $\ln(\dot{\varepsilon})$ determines the strain rate sensitivity. The effect of strain rate on the fracture strength of W5|7 GB with the 9.4° misorientation angle is shown in Figure 7. The higher the strain rate, the higher the strength of the material because there are fewer energy dissipating mechanisms active in the given strain rates of up to 10^{-8} s^{-1}. Furthermore, fracture strength is more strain rate sensitive at higher temperatures than at low temperatures, but it saturates at T≥200K. At higher strain rates, fracture strength is less temperature sensitive. At temperature below 200K, the fracture strength of monolayer WSe_2 GBs converges to the same value of $\ln(\sigma) \approx 3$ upon increasing to the strain rate of $\ln(\dot{\varepsilon}) \approx 24.5$.

Although we found a linear relationship between the strain rate and fracture stress at temperatures less than 300K, we revealed a nonlinear behaviour at the higher temperature of 350K. The fracture stress reached a plateau at an elevated temperature below a critical strain rate, possibly due to the higher contribution of thermal fluctuations to the formation of initial microcracks, determining the final fracture stress. While thermal fluctuations will not have time to contribute to the formation of microcracks at low temperatures, resulting in dominated loading rate behaviour, at lower strain rates, the initiation of microcracks will be determined by thermal fluctuations and thus become independent of the loading rate.

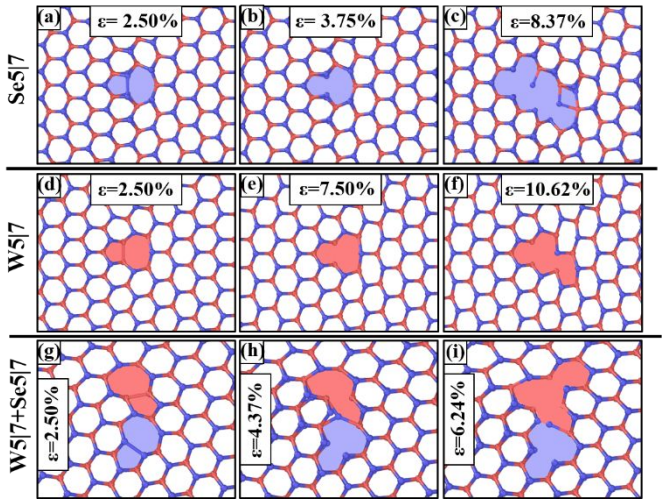

Figure 8. Kinetics of fracture for bicrystal WSe_2 structures with different GBs. (a-c) 9.4° Se5|7, (d-f) 9.4° W5|7, and (g-i) 44.6° W5|7+Se5|7. Snapshots are shown at different strains at 10K temperature. W5|7 and Se5|7 dislocations in GBs are painted red and blue, respectively. Red circles represent W atoms, and blue circles represent Se atoms.

Fracture process

The fracture mechanism of monolayer WSe_2 GB is quite different from that reported for single atomic graphene GB. For graphene, the rupture process starts by breaking the bond shared by the hexagon-heptagon ring [56,63] since the initial stress was maximum for the same bond. However, the initial compressive stress for the WSe_2 5|7 dislocation is maximum for the bond shared by 5|7 rings (Figure 8). That is the Se-Se bond for Se5|7 GBs and W-W bond for W5|7 GBs; see Figures 8 (b), (e), and (h). Although these bonds are under compressive stress, they break first instead of the ones under tension, i.e., single W atom of heptagon for Se5|7 GBs, double W atom of

the heptagon for W5|7 GBs. The Se-Se bond in Se5|7 GBs and W-W bond in W5|7 GBs cannot accommodate the external strains by bond rotation. Thus, although the pre-strained W-Se bond experiences the highest tensile stress, it still will not break as it can accommodate the external strain by rotating the W-Se bond, shown in Figure S5 in the Supplementary Information. The Se-Se bond in Se5|7 GBs breaks at a lower strain than the W-W bond in W5|7 GBs, which explains the higher failure strain for W5|7 AC tilt GB structures. Subsequently, the hexagon-heptagon ring dissociates, Figure 8, and cracks spread quickly along the GBs, explaining the sudden drop in stress-strain curves.

Conclusions

The role of GB defects with varying misorientation angles on the mechanical characteristics of WSe_2 at different temperatures was investigated using MD simulations. W5|7 and Se5|7 AC tilt GBs with misorientation angles of 9.4°, 13.2°, and 21.8° and one W5|7+Se5|7 ZZ tilt GB with misorientation angles of 39.4°, 44.6°, and 48.4° were studied within the 10K to 300K temperature range. Our results suggest that with increasing temperature, the fracture strength reduces for all the symmetric GB structures of WSe_2 due to the thermal activation of bond breakage and microcrack formation at higher temperatures. The effect of GB misorientation angle on fracture strength is noticeable at lower temperatures and reduced upon increasing temperature. The Misorientation angle changes the bond length and the internal stress state of the GB atoms and, thus, the strength at which the material fails. We have shown that AC tilt W5|7 GBs have a higher fracture strength than AC tilt Se5|7 and ZZ tilt W5|7+Se5|7 GBs. Furthermore, we revealed that the fracture strength of high angle ZZ tilt W5|7+Se5|7 GBs drops upon increasing the misorientation angle and become temperature insensitive. The young's modulus of both AC and ZZ tilt GBs also reduced and reached a plateau upon increasing temperature. Furthermore, we investigated the sensitivity of our results to the strain rate, indicating insensitivity of the results for temperatures above 200K. Also, the fracture strength of monolayer WSe_2 converged to a specific value for T<200K upon increasing the loading rate. The results presented here provide a fundamental understanding of the role of GBs in bi-atomic monolayers, such as TMDCs, on their final mechanical performance. Thus, it paves the way to design next-generation optoelectronic devices.

Author Contributions

Nuruzzaman Sakib: Methodology, Investigation, Formal analysis, Visualization, Writing - Original Draft**, Shiddartha Paul:** Writing - Review & Editing, **Nadire Nayir:** Writing - Review & Editing, **Adri C.T. van Duin:** Writing - Review & Editing, **Sara Neshani:** Writing - Review & Editing, **Kasra Momeni:** Conceptualization, Writing - Review & Editing, Supervision, Funding acquisition.

Conflicts of interest

There are no conflicts to declare.

Acknowledgements

This project is partly supported by DoE-ARPA-E OPEN (DE-AR0001066), the National Science Foundation 2D Crystal Consortium – Material Innovation Platform (2DCC-MIP) under NSF cooperative agreement DMR-1539916, the NSF-CAREER under NSF cooperative agreement CBET-2042683, and ATI and Mechanical Engineering Department of the University of Alabama.

References

1 R. Frisenda, Y. Niu, P. Gant, M. Muñoz and A. Castellanos-Gomez, Naturally occurring van der Waals materials, *npj 2D Mater. Appl. 2020 41*, 2020, **4**, 1–13.

2 K. S. Novoselov, D. Jiang, F. Schedin, T. J. Booth, V. V Khotkevich, S. V Morozov and A. K. Geim, Two-dimensional atomic crystals, *Proc. Natl. Acad. Sci. U. S. A.*, 2005, **102**, 10451–10453.

3 A. Castellanos-Gomez, Why all the fuss about 2D semiconductors?, *Nat. Photonics*, 2016, **10**, 202–204.

4 G. Fiori, F. Bonaccorso, G. Iannaccone, T. Palacios, D. Neumaier, A. Seabaugh, S. K. Banerjee and L. Colombo, Electronics based on two-dimensional materials, *Nat. Nanotechnol.*, 2014, **9**, 768–779.

5 S. Paul, R. Torsi, J. A. Robinson and K. Momeni, Effect of the Substrate on MoS2 Monolayer Morphology: An Integrated Computational and Experimental Study, *ACS Appl. Mater. & Interfaces*, 2022, **14**, 18835–18844.

6 Q. H. Wang, K. Kalantar-Zadeh, A. Kis, J. N. Coleman and M. S. Strano, Electronics and optoelectronics of two-dimensional transition metal dichalcogenides, *Nat. Nanotechnol.*, 2012, **7**, 699–712.

7 E. M. Vogel and J. A. Robinson, Two-dimensional layered transition-metal dichalcogenides for versatile properties and applications, *MRS Bull.*, 2015, **40**, 558–563.

8 N. Briggs, S. Subramanian, Z. Lin, X. Li, X. Zhang, K. Zhang, K. Xiao, D. Geohegan, R. Wallace, L.-Q. Chen, M. Terrones, A. Ebrahimi, S. Das, J. Redwing, C. Hinkle, K. Momeni, A. van Duin, V. Crespi, S. Kar and J. A. Robinson, A roadmap for electronic grade 2D materials, *2D Mater.*, 2019, **6**, 022001.

9 K. Momeni, Y. Ji, Y. Wang, S. Paul, S. Neshani, D. E. Yilmaz, Y. K. Shin, D. Zhang, J.-W. W. Jiang, H. S. Park, others, S. Sinnott, A. van Duin, V. Crespi and L. Q. Chen, *Multiscale computational understanding and growth of 2D materials: a review*, Nature Publishing Group, 2020, vol. 6.

10 R. A. Vilá, K. Momeni, Q. Wang, B. M. Bersch, N. Lu, M. J. Kim, L. Q. Chen and J. A. Robinson, Bottom-up synthesis of vertically oriented two-dimensional materials, *2D Mater.*, 2016, **3**, 041003.

11 F. Zhang, K. Momeni, M. A. AlSaud, A. Azizi, M. F. Hainey, J. M. Redwing, L.-Q. Chen and N. Alem, Controlled synthesis of 2D transition metal dichalcogenides: from vertical to planar MoS 2, *2D Mater.*, 2017, **4**, 025029.

12 K. Momeni, Y. Ji, K. Zhang, J. A. Robinson and L.-Q. Chen, Multiscale framework for simulation-guided growth of 2D materials, *npj 2D Mater. Appl.*, 2018, **2**, 27.

13 Y. Ji, K. Momeni and L.-Q. Chen, A multiscale insight into the growth of h-BN: effect of the enclosure, *2D Mater.*, 2021, **8**, 035033.

14 D. Akinwande, N. Petrone and J. Hone, Two-dimensional flexible nanoelectronics, *Nat. Commun.*, 2014, **5**, 5678.

15 A. A. Balandin, S. Ghosh, W. Bao, I. Calizo, D. Teweldebrhan, F. Miao and C. N. Lau, Superior Thermal Conductivity of Single-Layer Graphene, *Nano Lett.*, 2008, **8**, 902–907.

16 R. R. Nair, P. Blake, A. N. Grigorenko, K. S. Novoselov, T. J. Booth, T. Stauber, N. M. R. Peres and A. K. Geim, Fine structure constant defines visual transparency of graphene., *Science (80-.).*, 2008, **320**, 1308.

17 C. Lee, X. Wei, J. W. Kysar and J. Hone, Measurement of the Elastic Properties and Intrinsic Strength of Monolayer Graphene, *Science (80-.).*, 2008, **321**, 385–388.

18 M. Munther, M. Shaygan, A. Centeno, D. Neumaier, A. Zurutuza, K. Momeni and K. Davami, Probing the mechanical properties of vertically-stacked ultrathin graphene/Al <inf>2</inf> O <inf>3</inf> heterostructures, *Nanotechnology*, , DOI:10.1088/1361-6528/aafd53.

19 S. Paul and K. Momeni, Mechanochemistry of Stable Diamane and Atomically Thin Diamond Films Synthesis from Bi- and Multilayer Graphene: A Computational Study, *J. Phys. Chem. C*, 2019, **123**, 15751–15760.

20 S. Paul, K. Momeni and V. I. Levitas, Shear-induced diamondization of multilayer graphene structures: A computational study, *Carbon N. Y.*, 2020, **167**, 140–147.

21 P. Rani and V. K. Jindal, Designing band gap of graphene by B and N dopant atoms, *RSC Adv.*, 2012, **3**, 802–812.

22 S. Ahmed and J. Yi, Two-Dimensional Transition Metal Dichalcogenides and Their Charge Carrier Mobilities in Field-Effect Transistors, *Nano-Micro Lett. 2017 94*, 2017, **9**, 1–23.

23 L. Yu, A. Zubair, E. J. G. Santos, X. Zhang, Y. Lin, Y. Zhang and T. Palacios, High-Performance WSe2 Complementary Metal Oxide Semiconductor Technology and Integrated Circuits, *Nano Lett.*, 2015, **15**, 4928–4934.

24 W. Zhao, Z. Ghorannevis, L. Chu, M. Toh, C. Kloc, P.-H. Tan and E. † Goki, Evolution of Electronic Structure in Atomically Thin Sheets of WS 2 and WSe 2, , DOI:10.1021/nn305275h.

25 R. Gatensby, N. McEvoy, K. Lee, T. Hallam, N. C. Berner, E. Rezvani, S. Winters, M. O'Brien and G. S. Duesberg, Controlled synthesis of transition metal dichalcogenide thin films for electronic applications, *Appl. Surf. Sci.*, 2014, **297**, 139–146.

26 Z. Song, T. Schultz, Z. Ding, B. Lei, C. Han, P. Amsalem, T. Lin, D. Chi, S. L. Wong, Y. J. Zheng, M. Y. Li, L. J. Li, W. Chen, N. Koch, Y. L. Huang and A. T. S. Wee, Electronic Properties of a 1D Intrinsic/p-Doped Heterojunction in a 2D Transition Metal Dichalcogenide Semiconductor, *ACS Nano*, 2017, **11**, 9128–9135.

27 C. K. Sumesh, Towards efficient photon management in nanostructured solar cells: Role of 2D layered transition metal dichalcogenide semiconductors, *Sol. Energy Mater. Sol. Cells*, 2019, **192**, 16–23.

28 J. S. Ross, P. Klement, A. M. Jones, N. J. Ghimire, J. Yan, D. G. Mandrus, T. Taniguchi, K. Watanabe, K. Kitamura, W. Yao, D. H. Cobden and X. Xu, Electrically tunable excitonic light-emitting diodes based on monolayer WSe2 p–n junctions, *Nat. Nanotechnol. 2014 94*, 2014, **9**, 268–272.

29 H. Fang, S. Chuang, T. C. Chang, K. Takei, T. Takahashi and A. Javey, High-performance single layered WSe 2 p-FETs with chemically doped contacts, *Nano Lett.*, 2012, **12**, 3788–3792.

30 H. Zhou, C. Wang, J. C. Shaw, R. Cheng, Y. Chen, X. Huang, Y. Liu, N. O. Weiss, Z. Lin, Y. Huang and X. Duan, Large area growth and electrical properties of p-type WSe2 atomic layers, *Nano Lett.*, 2015, **15**, 709–713.

31 S. M. Eichfeld, L. Hossain, Y.-C. Lin, A. F. Piasecki, B. Kupp, A. G. Birdwell, R. A. Burke, N. Lu, X. Peng, J. Li, A. Azcatl, S. McDonnell, R. M. Wallace, M. J. Kim, T. S. Mayer, J. M. Redwing and J. A. Robinson, Highly Scalable, Atomically Thin WSe 2 Grown via Metal–Organic Chemical Vapor Deposition, *ACS Nano*, 2015, **9**, 2080–2087.

32 J. Huang, L. Yang, D. Liu, J. Chen, Q. Fu, Y. Xiong, F. Lin and B. Xiang, Large-area synthesis of monolayer WSe 2 on a SiO 2 /Si substrate and its device applications, *Nanoscale*, 2015, **7**, 4193–4198.

33 L. Chen, B. Liu, A. N. Abbas, Y. Ma, X. Fang, Y. Liu and C. Zhou, Screw-Dislocation-Driven growth of Two-Dimensional few-layer and pyramid-like WSe2by sulfur-assisted Chemical Vapor Deposition, *ACS Nano*, 2014, **8**, 11543–11551.

34 J.-K. Huang, J. Pu, C.-L. Hsu, M.-H. Chiu, Z.-Y. Juang, Y.-H. Chang, W.-H. Chang, Y. Iwasa, T. Takenobu and L.-J. Li, Large-Area Synthesis of Highly Crystalline WSe 2 Monolayers and Device Applications, *ACS Nano*, 2014, **8**, 923–930.

35 F. Banhart, J. Kotakoski and A. V Krasheninnikov, Structural Defects in Graphene, *ACS Nano*, 2011, **5**, 26–41.

36 M. Tripathi, F. Lee, A. Michail, D. Anestopoulos, J. G. McHugh, S. P. Ogilvie, M. J. Large, A. A. Graf, P. J. Lynch, J. Parthenios, K. Papagelis, S. Roy, M. A. S. R. Saadi, M. M. Rahman, N. M. Pugno, A. A. K. King, P. M. Ajayan and A. B. Dalton, Structural Defects Modulate Electronic and Nanomechanical Properties of 2D Materials, *ACS Nano*, 2021, **15**, 2520–2531.

37 Z. Islam, A. Kozhakhmetov, J. Robinson and A. Haque, Enhancement of WSe2 FET Performance Using Low-Temperature Annealing, *J. Electron. Mater.*, , DOI:10.1007/s11664-020-08087-w.

38 W. Su, N. Kumar, H. Shu, O. Lancry and M. Chaigneau, In Situ Visualization of Optoelectronic Behavior of Grain Boundaries in Monolayer WSe2 at the Nanoscale, *J. Phys. Chem. C*, 2021, **125**, 26883–26891.

39 Z. Wu and Z. Ni, Spectroscopic investigation of defects in two-dimensional materials, *Nanophotonics*, 2017, **6**, 1219–1237.

40 A. Falin, M. Holwill, H. Lv, W. Gan, J. Cheng, R. Zhang, D. Qian, M. R. Barnett, E. J. G. Santos, K. S. Novoselov, T. Tao, X. Wu and L. H. Li, Mechanical Properties of Atomically Thin Tungsten Dichalcogenides: WS 2 , WSe 2 , and WTe 2, *ACS Nano*, 2021, **15**, 2600–2610.

41 E. H. Chowdhury, M. H. Rahman, S. Fatema and M. M. Islam, Investigation of the mechanical properties and fracture mechanisms of graphene/WSe2 vertical heterostructure: A molecular dynamics study, *Comput. Mater. Sci.*, 2021, **188**, 110231.

42 Z. Islam and A. Haque, Defects and grain boundary effects in MoS2: A molecular dynamics study, *J. Phys. Chem. Solids*, 2021, **148**, 109669.

43 W. Ding, D. Han, J. Zhang and X. Wang, Mechanical responses of WSe 2 monolayers: a molecular dynamics study, *Mater. Res. Express*, 2019, **6**, 085071.

44 K. Q. Dang and D. E. Spearot, Effect of point and grain boundary defects on the mechanical behavior of monolayer MoS 2 under tension via atomistic simulations, *J. Appl. Phys.*, 2014, **116**, 013508.

45 N. Nayir, Y. Wang, S. Shabnam, D. R. Hicke, L. Miao, X. Zhang, S. Bachu, N. Alem, J. Redwing and V. H. Crespi, Modeling for structural engineering and synthesis of two-dimensional WSe2 using a newly developed Reaxff reactive force field, *J. Phys. Chem. C*, 2020, **124**, 28285–28297.

46 R. Abadi, R. P. Uma, M. Izadifar and T. Rabczuk, The effect of temperature and topological defects on fracture strength of grain boundaries in single-layer polycrystalline boron-nitride nanosheet, *Comput. Mater. Sci.*, 2016, **123**, 277–286.

47 A. P. Thompson, H. M. Aktulga, R. Berger, D. S. Bolintineanu, W. M. Brown, P. S. Crozier, P. J. in 't Veld, A. Kohlmeyer, S. G. Moore, T. D. Nguyen, R. Shan, M. J. Stevens, J. Tranchida, C. Trott and S. J. Plimpton, LAMMPS - a flexible simulation tool for particle-based materials modeling at the atomic, meso, and continuum scales, *Comput. Phys. Commun.*, 2022, **271**, 108171.

48 X. Zhou, X. Liu, F. Sansoz and M. Shen, Molecular dynamics simulation on temperature and stain rate-dependent tensile response and failure behavior of Ni-coated CNT/Mg composites, *Appl. Phys. A Mater. Sci. Process.*, 2018, **124**, 1–11.

49 T. S. Akash, R. A. S. I. Subad, P. Bose and M. M. Islam, Nanomechanics of antimonene allotropes under tensile loading, *Phys. Chem. Chem. Phys.*, 2021, **23**, 6241–6251.

50 S. Deng, L. Li and M. Li, Stability of direct band gap under mechanical strains for monolayer MoS2, MoSe2, WS2 and WSe2, *Phys. E Low-dimensional Syst. Nanostructures*, 2018, **101**, 44–49.

51 A. Sadeghirad, K. Momeni, Y. Ji, X. Ren, L.-Q. L. Q. Chen and J. Lua, Multiscale crystal-plasticity phase field and extended finite element methods for fatigue crack initiation and propagation modeling, *Int. J. Fract.*, 2019, **216**, 41–57.

52 J. C. M. Li, Disclination model of high angle grain boundaries, *Surf. Sci.*, 1972, **31**, 12–26.

53 A. E. Romanov and A. L. Kolesnikova, Application of disclination concept to solid structures, *Prog. Mater. Sci.*, 2009, **54**, 740–769.

54 M. Kleman and J. Friedel, Disclinations, dislocations, and continuous defects: A reappraisal, *Rev. Mod. Phys.*, 2008, **80**, 61–115.

55 T. H. Liu, C. W. Pao and C. C. Chang, Effects of dislocation densities and distributions on graphene grain boundary failure strengths from atomistic simulations, *Carbon N. Y.*, 2012, **50**, 3465–3472.

56 R. Grantab, V. B. Shenoy and R. S. Ruoff, Anomalous Strength Characteristics of Tilt Grain Boundaries in Graphene, *Science (80-.).*, 2010, **330**, 946 LP – 948.

57 Y. I. Jhon, S. E. Zhu, J. H. Ahn and M. S. Jhon, The mechanical responses of tilted and non-tilted grain boundaries in graphene, *Carbon N. Y.*, 2012, **50**, 3708–3716.

58 L. Yang, J. Liu, Y. Lin, K. Xu, X. Cao, Z. Zhang and J. Wu, Strengthening and Weakening by Dislocations in Monolayer MoS 2, *Chem. Mater.*, 2021, **33**, 8758–8767.

59 H. Zhang, Z. Duan, X. Zhang, C. Liu, J. Zhang and J. Zhao, Strength and fracture behavior of graphene grain boundaries: Effects of temperature, inflection, and symmetry from molecular dynamics, *Phys. Chem. Chem. Phys.*, 2013, **15**, 11794–11799.

60 J. W. Jiang, J. S. Wang and B. Li, Young's modulus of graphene: A molecular dynamics study, *Phys. Rev. B - Condens. Matter Mater. Phys.*, 2009, **80**, 113405.

61 A. Mobaraki, A. Kandemir, H. Yapicioglu, O. Gülseren and C. Sevik, Validation of inter-atomic potential for WS2 and WSe2 crystals through assessment of thermal transport properties, *Comput. Mater. Sci.*, 2018, **144**, 92–98.

62 C. M. Sellars and W. J. McTegart, On the mechanism of hot deformation, *Acta Metall.*, 1966, **14**, 1136–1138.

63 J. Wu and Y. Wei, Grain misorientation and grain-boundary rotation dependent mechanical properties in polycrystalline graphene, *J. Mech. Phys. Solids*, 2013, **61**, 1421–1432.